Identifying DQ-Domain Admittance Models of a 2.3-MVA Commercial Grid-Following Inverter Via Frequency-Domain and Time-Domain Data

Lingling Fan, *Senior Member, IEEE*, Zhixin Miao, *Senior Member, IEEE*, Przemyslaw Koralewicz, *Member, IEEE*, Shahil Shah, *Member, IEEE*, and Vahan Gevorgian, *Senior Member, IEEE*

***Abstract*—In this paper, we present two methods to identify the admittance of a 2.3-MVA commercial grid-following inverter through frequency-domain data and time-domain data. In addition to the well-known harmonic injection method to obtain the admittance at frequency points followed by vector fitting, we adopt a step response-based method where the step response data of the converter are collected and their s-domain expressions are obtained. In turn, the s-domain admittance model of the converter is found. The two methods can be used for cross validation. Step responses and frequency-domain responses obtained from the two methods are compared. Results show that the time-domain data-based method leads to an admittance comparable with that from the frequency-domain measurement in the range less than 60 Hz. In addition, two insights are obtained from the frequency-domain admittance measurements. First, when the dq-frame is aligned to the point of common coupling (PCC) voltage, the per unit DQ-domain admittance directly reflects operating conditions. Second, existence of negative-sequence control can be detected via sequence-domain admittances.**

***Index Terms*—Admittance; grid-following inverter; frequency scan; system identification**

I. Introduction

MORE and more wind and solar are being integrated into power grids. Unlike conventional generators, which rely on a rotating magnetic field to convert mechanical energy to electric energy and which can be directly connected to an ac grid, solar and wind rely on power electronic converters as the interface to the grid. They are called inverter-based resources (IBRs).

High penetrations of IBRs significantly change grid dynamic characteristics. Unprecedented dynamics have occurred in power grids. Examples include 20–30-Hz oscillations that occurred in 2009 and 2017 in Texas when wind farms radially connected to series capacitors [1], 9-Hz oscillations that occurred in August 2019 in an offshore wind farm in the United Kingdom before the power disruption [2], and subcyle overvoltage dynamics that triggered large-scale solar photovoltaic tripping in California in 2017 and 2018 [3].

A hurdle to the dynamic study of IBR grid integration systems is that IBRs are black boxes because of proprietary information; thus, impedance or admittance-based stability analysis has become attractive for the grid industry because impedance/admittance can be characterized via measurement [1]. Impedance-based stability analysis has proven effective for the evaluation of control interactions and stability problems involving IBRs [4], [5].

This paper presents the admittance measurement of a utility-scale 2.3-MVA inverter using a 13.8-kV/7-MW grid simulator called the controllable grid interface (CGI) at the Flatirons Campus of the National Renewable Energy Laboratory (NREL). The admittance of an inverter can be measured by injecting voltage at different frequencies from its terminals superimposed on the voltages at the fundamental frequency. Such perturbations excite the inverter dynamics over a broad frequency range. In the literature, this method is referred to as the well-known harmonic injection method or the frequency-scanning method [6], [7].

The sine-signal injection frequency-domain measurement is known for accuracy. However, it is also known as time consuming. Thus, we also implement a time-domain measurement-based method, which relies on step response data generated by two experiments at minimum. The concept of the method has been presented in [8], along with demonstrations in computer simulation environment. This paper reports the first-time implementation of the proposed time-domain method in a MW-level hardware test bed.

With two measurement methods, cross validation is conducted via two approaches. In the first approach, vector fitting [9] is applied to fit the frequency-domain measurement to a linear model. This model is then subject to step changes. Its step responses are compared with the time-domain measurement data.

In the second approach, system identification is carried out using the time-domain data to lead to an admittance model. The frequency-domain responses of the admittance model are compared with the frequency-domain measurements.

This work was authored in part by the National Renewable Energy Laboratory, operated by Alliance for Sustainable Energy, LLC, for the U.S. Department of Energy (DOE) under Contract No. DE-AC36-08GO28308.

This material is based upon work supported by the U.S. Department of Energy's Office of Energy Efficiency and Renewable Energy (EERE) under the Solar Energy Technologies Office Award Number DE-EE0008771.

L. Fan and Z. Miao are with Dept. of Electrical Engineering, University of South Florida, Tampa FL 33620 (email: linglingfan@usf.edu; zmiao@usf.edu).

P. Koralewicz, S. Shah, and V. Gevorgian are with the National Renewable Energy Laboratory, Golden, CO 80401 USA (e-mails: przemyslaw.koralewicz@nrel.gov; Shahil.Shah@nrel.gov; vahan.gevorgian@nrel.gov).

In the second approach, time-domain measurement data-based model identification is used to find the DQ-domain impedance. This method is more efficient because it requires only two experiments at minimum, as shown in [10]. In [10], two sets of event data are recorded following post-processing to filter out noise. The data are then fed to a system identification algorithm: the output error method. This leads to an input and output model. However, an excellent match is still lacking, as shown in the comparison results in Fig. 8 of in [10].

Most recently, a time-domain data-based method relying on subspace identification was proposed in [8], [11]. It was shown to arrive at an excellent match for the model output versus the measurement data. Tests have been conducted for data generated from electromagnetic transient simulation test beds. In this research, this method will also be adopted for admittance measurement for the 2.3-MVA inverter.

Thus, the main work of this paper is to identify the DQ-domain admittance of a 2.3-MVA inverter using both frequency-domain data and time-domain data.

Because admittance is essentially a linearized model based on an operating condition, different operating conditions have been considered in the measuring process, and their influence on admittance is demonstrated and analyzed. It is found that for DQ-domain admittance, low-frequency admittance response indeed reflects the operating condition. In addition, whether unbalanced control has been included can be predicted from the admittance models.

The contribution of this paper is twofold.

- We not only obtain frequency-domain admittance measurement data of a 2.3-MVA commercial converter at various operating conditions using advanced hardware, but also draw two important insights from the per unitized frequency-domain admittance measurements. The first insight is that the low-frequency admittance measurement in a dq-frame aligned to the PCC voltage directly reflects P, Q operating conditions. The second insight is that the existence of the unbalanced control can be detected after converting the DQ-domain admittance to the sequence-domain admittance.
- We implement a transient response data-based admittance model identification method in a MW-level hardware test bed. Compared to the frequency scanning method, the proposed method requires few experiments. This research leads to valuable experience in utilizing transient response data for admittance identification in real world. Further, feasibility and limitations of the time-domain method are identified.

To the best of the authors' knowledge, the two insights have not been stated in the state-of-the-art. In addition, the transient response data-based method is not a conventional wide-band signal injection method seen in the literature. The existing methods relying on wide-band signal injections, e.g., impulse signal [12], [13], chirp signals [14], pseudo-random binary sequence signals [15], and ternary-sequence signals [16], can be classified as frequency-domain methods since discrete Fourier transform (DFT) is used to obtain frequency-domain data.

A significant difference between the proposed time-domain method versus those frequency-domain methods is that Fourier transform of measurement data is not used. The prposed method views the transient response data as the output of a linear time invariant (LTI) dynamic system expressed as $\dot{x} = Ax$. It relies on data analytics methods, e.g., dynamic mode decomposition (DMD), to extract the LTI system information from a large-size data Hankel matrix. This Hankel matrix is based on time-domain measurements. The information obtained from DMD includes the system matrix A, its eigenvalues, and residues. With the information of the LTI model, s-domain expressions of measurement data are found. In the experiment design, with the voltage perturbation's s-domain expressions known and the current response s-domain expressions found, admittance models are identified.

The remainder of the paper is organized as follows. Section II describes the measurement test bed. Section III presents the frequency-domain and time-domain measurement data. Section IV presents the cross-validation results. Section V presents insights obtained from the admittance responses. Section VI concludes this paper.

II. The Measurement Test Bed

A 2.3-MVA inverter driven by a 1-MW battery will be measured for its admittance. The control structure of the inverter is not known. The inverter can follow real power order and reactive power order. Thus, this converter is a grid-following voltage source converter operating in real power and reactive power regulation mode.

This converter is connected to a 13.8-kV/7-MW grid simulator, or the CGI [17], via a 400-V/13.2-kV 1-MVA step-up transformer. The CGI is operating at 13.2 kV. Fig. 1 presents the measurement test bed constructed at NREL. The circuit parameters are given in the caption. The measurement point is at the grid bus or at the CGI and the dq-frame is chosen to be aligned with the measurement point voltage exactly or the PCC voltage approximately; thus, the admittance includes the RC filter at 13.2 kV, the transformer, and the shunt cap at 400 V.

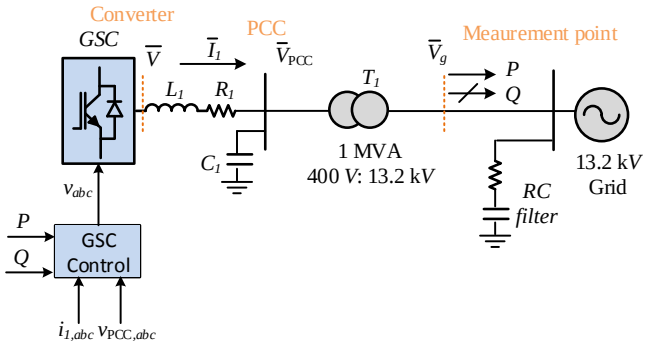

Fig. 1: The admittance measurement test bed. The dq-frame is aligned with the grid voltage. The RC filter parameters are: $R = 15\,\Omega$, and $C = 6.39\,\mu$F. The transformer's per-unit impedance is $0.02 + j0.0721$. The 400-V capacitor parameter is $444\,\mu$F. The RL filter parameters are $R_1 = 0.001\,\Omega$ and $L_1 = 46 \times 10^{-6}$ H.

Per-unit analysis is conducted for the circuit for a power base of 1-MVA. For the 13.2-kV system, the RC filter's admittance per-unit value is:

$$Y_{\text{RC}} = \frac{Z_b}{R - jX_c} = \frac{\frac{13.2^2}{1}}{15 - j\frac{1}{377\times 6.39\times 10^{-6}}} = 0.0151 + j0.4192. \quad (1)$$

Thus, at the nominal voltage, the reactive power sent by the RC filter is approximately 0.4 p.u. or 400 kVAr.

1) Grid Simulator: The CGI at NREL is shown in Fig. 2. It is rated for 13.8-kV, 7-MVA continuous power, and it has a 39-MVA short-term rating for 2 seconds. It is custom-designed based on ABB's ACS6000 industrial-grade medium-voltage drive technology. It features a 9-MVA active rectifier unit at the utility side that regulates the intermediate dc bus voltage. The controllable grid is established by four front-end neutral-point-clamped inverters, each with a rated output of 3.3 kV, connected in parallel. A specialized multi-winding output transformer, also shown in Fig. 2, is used to synthesize 17-level low-distortion voltage waveforms by combining three-level phase voltages from the inverters. The transformer also steps up the voltage to 13.8 kV. The CGI is designed to simultaneously meet the following requirements: multimegawatt power rating, sub-1% total harmonic distortion in the voltage waveforms, and an extremely fast response time of less than 1 ms. The fast dynamics of the CGI enable it to behave like an ideal voltage source that can be used for transient experiments and to inject perturbations over a broad frequency range for impedance measurements. The control system of the CGI is coupled with a Real-Time Digital Simulator (RTDS), which can provide dynamic voltage references for all three phases and the neutral wire for different grid integration tests; the desired perturbation for admittance measurement of the 2.3-MVA inverter is configured inside the RTDS.

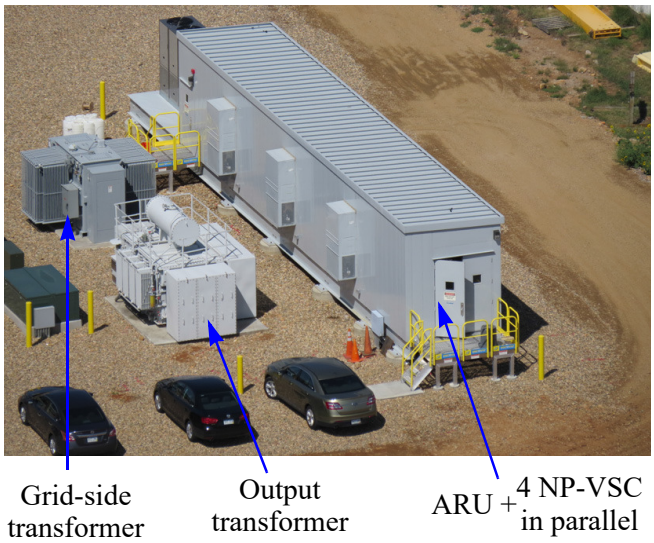

Fig. 2: T13.8-kV/7-MVA grid simulator, called a controllable grid interface (CGI), custom designed using ABB's medium-voltage ACS6000 drive technology. Source: Mark McDade, NREL.

III. Measurement Data: Frequency-Domain and Time-Domain

A. Frequency-Domain Measurements

Fig. 3 presents the Bode plots of the dq-admittance measured by the CGI at four different operating conditions. This admittance is viewed at the CGI, and thus it includes the effect of the RC filter. The CGI sets the supplying voltage in steady-state as $1\angle 0$ p.u.. The four operating conditions are:

- Case 1: $P = 0$ kW, $Q = 0$ kVAr
- Case 2: $P = 500$ kW, $Q = 0$ kVAr
- Case 3: $P = 0$ kW, $Q = 500$ kVAr
- Case 4: $P = 1000$ kW, $Q = 0$ kVAr

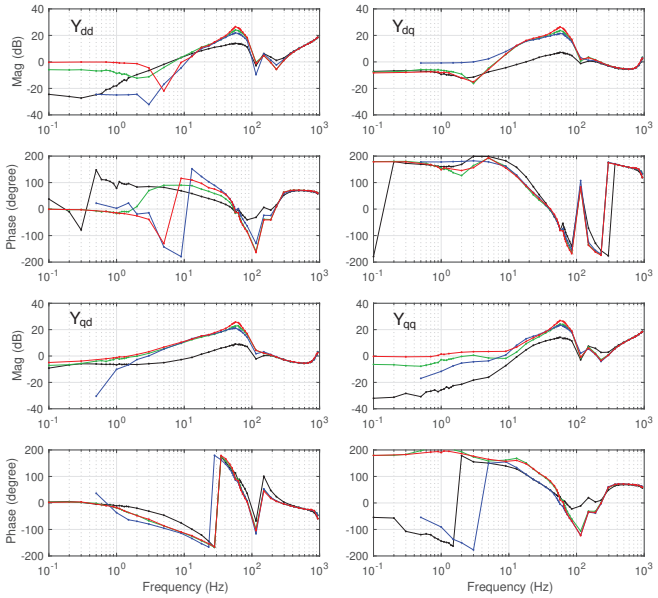

Fig. 3: The measured DQ-domain admittance after being per unitized. The four operating conditions are represented by different colors —Case 1: black. Case 2: green. Case 3: blue. Case 4: red.

The effect of the RC filter can be easily removed by subtracting the RC filter's admittance from the measured admittance. Fig. 4 presents the DQ-domain admittance viewed at the measurement point.

B. Time-Domain Measurement Data

The experiments are designed for three operating conditions: Case 1, Case 2, and Case 3. For each operating condition, two experiments are conducted for the same step change size: v_d step-down and v_q step-up. For each experiment, currents flowing out of the converter, i_d and i_q, are recorded. A series of step change sizes are used: 1%, 2%, 5%, 10%, 15%, 20%, 30%, 40%, and 50%.

The CGI outputs three-phase voltages with the magnitude and angle programmable. In the initial steady state, the CGI's voltage is operating in nominal condition with the phase angle at 0. To have a 10% v_d step-down, the magnitude of the voltage will be changed from 1 to 0.9. In order to have 10% v_q step-up, both the magnitude and the angle need to be changed. As

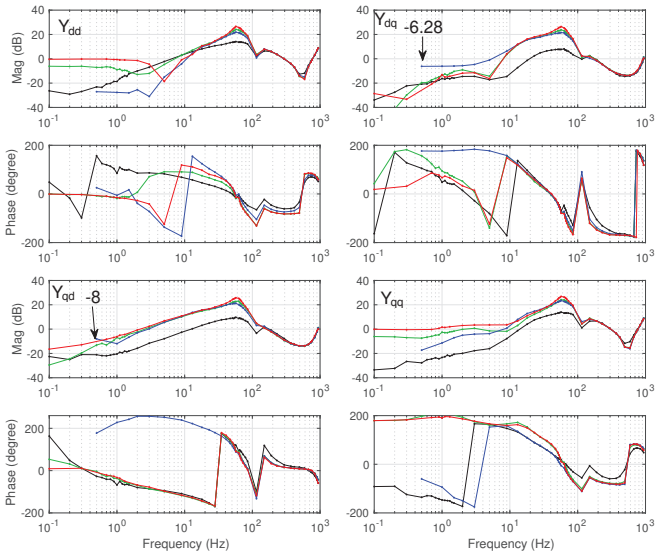

Fig. 4: The DQ-domain admittance viewed at the measurement point.

shown in the following, the magnitude is increased from 1 to 1.005, and the angle increases from 0 to 5.7°:

$$\overline{V} = 1 + j0.1 = 1.005\underline{/5.7°}. \tag{2}$$

Fig. 5 presents the input and output data for the experiments in the Case 1 operating condition when the inverter delivers 0 real and reactive power. The presented data are the filtered data after a third-order Butterworth filter with 500-Hz bandwidth.

Results show that in the initial condition, the CGI voltage is at $v_d = 1$ and $v_q = 0$. Fig. 5(a) presents the v_d step change data, and Fig. 5 presents the v_q step change data. Three step sizes are used: 5%, 10%, and 15%.

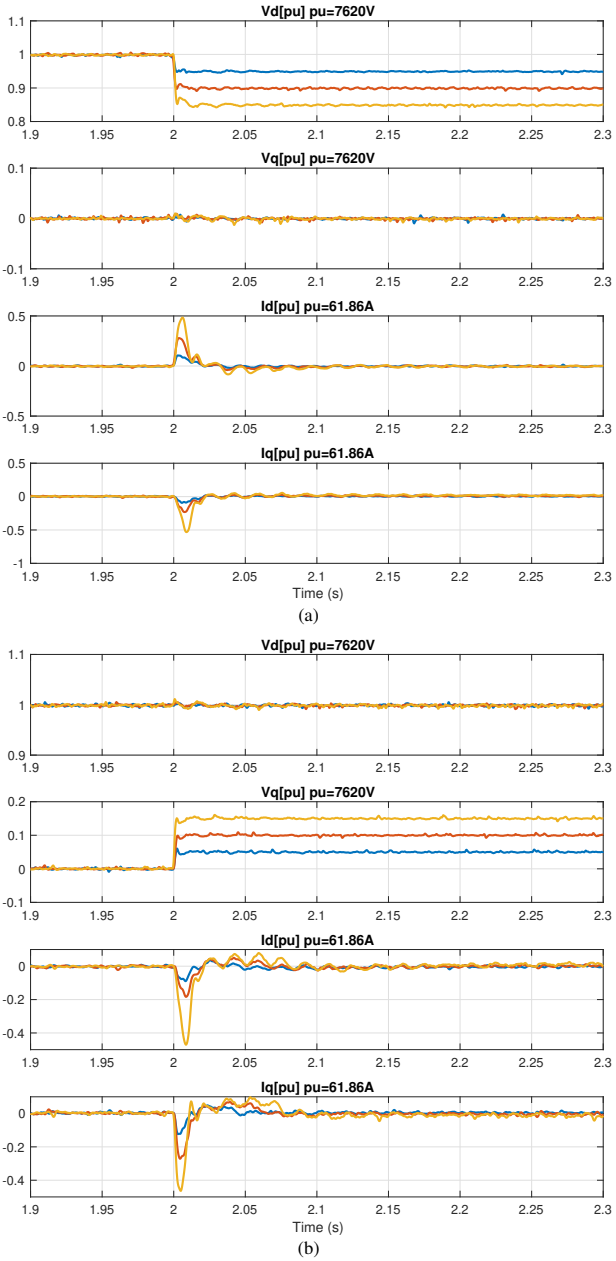

Fig. 5: (a) Event 1: step change in v_d. (b) Event 2: step change in v_q.

IV. Cross Validation

A. First Approach: Step Response Comparison

1) Vector-Fitting Results: For each operating condition, approximately 50 measurement frequency points are selected to conduct harmonic injection, time-domain data recording, and Fourier transformation. The resulting admittance is a set of measurement points instead of a linear model. To arrive at a linear state-space model or a transfer function matrix, the vector-fitting method [9] is applied to the measurement data. The MATLAB toolbox is available in the public domain for research. A system can be represented as a transfer function matrix with each transfer function represented by a numerator and a denominator. Both numerator and denominator are polynomials of the Laplace operator, s. Vector fitting is essentially a least-squares estimation method to estimate the numerator and denominator's coefficients by minimizing the sum of the squared errors between the model output and the measurements.

To start the method, the model's order or the system's rank is first chosen along with the poles of the system. Through iterations, the model and the measurement data achieve a high-degree match. In this example, the four linear systems corresponding to the four operating conditions are found using the Y_{dd}, Y_{dq}, Y_{qd}, and Y_{qq} measurement data. The orders of the systems are all assumed to be 16.

Fig. 6 presents the comparison between the admittance model obtained from vector fitting and the measurement data. As shown, high-degree matching is obtained.

2) Comparison with the Time-Domain Data: Fig. 7 presents the comparison of the measured step response data for the 10% and 20% step changes and the step response generated by the models obtained after vector fitting. Results show that the models generate comparable step responses.

B. Second Approach: Frequency-Domain Response Comparison

In this approach, the admittance models will be identified based on the measured step response data. Our approach is to

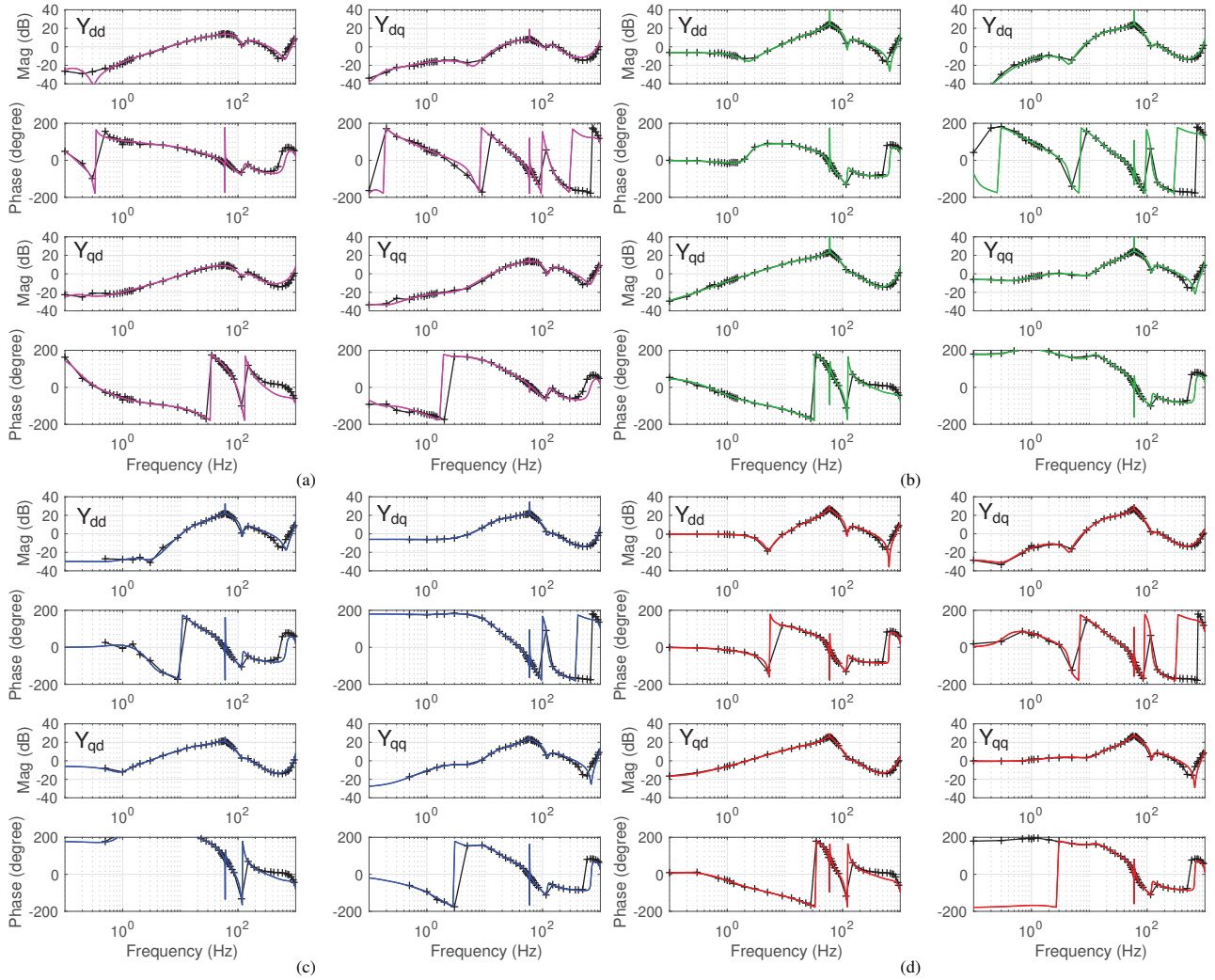

Fig. 6: Comparison of the admittance model from vector fitting and the admittance measurement points. Solid lines: vector fitting. Crosses: discrete frequency-domain measurements.

find the s-domain expression of the currents using the system identification algorithm. Because the inputs are voltage step changes with their transfer functions known, the s-domain admittance can be found by using the following procedure.

The inverter's current flowing out and its terminal voltage are related to its admittance as follows:

$$\begin{bmatrix} -i_d(s) \\ -i_q(s) \end{bmatrix} = \underbrace{\begin{bmatrix} Y_{dd}(s) & Y_{dq}(s) \\ Y_{qd}(s) & Y_{qq}(s) \end{bmatrix}}_{Y} \begin{bmatrix} v_d(s) \\ v_q(s) \end{bmatrix}, \tag{3}$$

where Y is the admittance of the inverter.

For Event 1, we have v_q not perturbed but v_d perturbed with a step-down change $\frac{-p}{s}$ where p is the perturbation size. Then the resulting responses, $i_d^{(1)}(s)$ and $i_q^{(1)}(s)$, should reflect the first column of the Y matrix: $Y_{dd}(s)$ and $Y_{qd}(s)$.

$$\begin{bmatrix} -i_d^{(1)}(s) \\ -i_q^{(1)}(s) \end{bmatrix} = \begin{bmatrix} Y_{dd}(s) & Y_{dq}(s) \\ Y_{qd}(s) & Y_{qq}(s) \end{bmatrix} \begin{bmatrix} (-p/s) \\ 0 \end{bmatrix} = \begin{bmatrix} Y_{dd}(s) \\ Y_{qd}(s) \end{bmatrix} \frac{-p}{s} \tag{4}$$

Similarly, for Event 2 where v_d is not perturbed while v_q is perturbed with a step-up change $\frac{p}{s}$, the relation becomes:

$$\begin{bmatrix} -i_d^{(2)}(s) \\ -i_q^{(2)}(s) \end{bmatrix} = \begin{bmatrix} Y_{dd}(s) & Y_{dq}(s) \\ Y_{qd}(s) & Y_{qq}(s) \end{bmatrix} \begin{bmatrix} 0 \\ (-p/s) \end{bmatrix} = \begin{bmatrix} Y_{dq}(s) \\ Y_{qq}(s) \end{bmatrix} \frac{-p}{s}. \tag{5}$$

Thus,

$$Y = \frac{s}{p} \begin{bmatrix} i_d^{(1)}(s) & -i_d^{(2)}(s) \\ i_q^{(1)}(s) & -i_q^{(2)}(s) \end{bmatrix}, \tag{6}$$

where the superscript (i) notates events.

To find the s-domain expressions for the four currents, system identification algorithms will be applied. Ho and Kalman, in 1965 [18], have discovered the seminal state-space realization theory: from measurement data, an LTI system's state-space model can be recovered.

We view the linearized models for the same operating condition subject to Event 1 and Event 2 are the same. Thus, we may use the four measurements $i_d^{(1)}(t)$, $i_q^{(1)}(t)$, $i_d^{(2)}(s)$ and $i_q^{(2)}(s)$generated from v_d perturbation and v_q perturbation to identify an LTI model. In addition, data from both 5% and 10% perturbation levels are used. Thus, the data Hankel matrix has

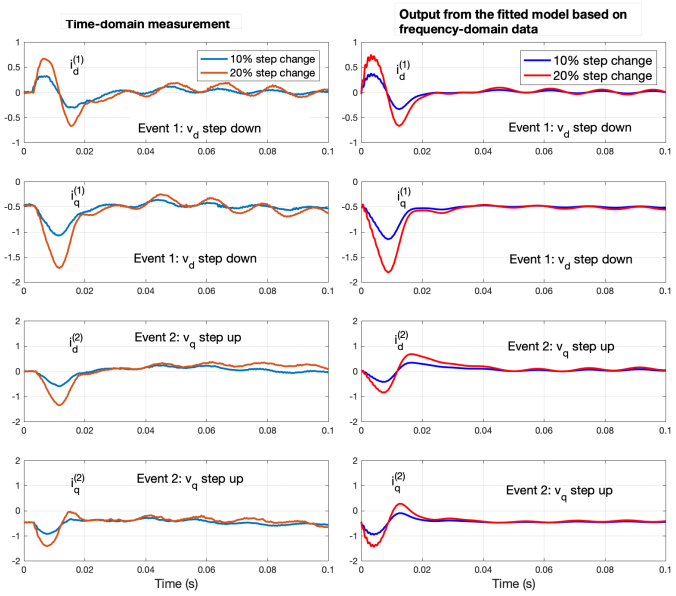

Fig. 7: Comparison of step responses: measurement (left panel) and the output of the fitted model based on the frequency-domain data (right panel). Operating condition: Case 3, $P = 0$, $Q = 0.5$ p.u..

a row dimension of 8. Its column dimension is same as the number of samples.

The sampling frequency 5,000-Hz and 0.8-second data starting from $t = 2$ are used. The resulting column dimension is 4,000. In this research, the DMD algorithm is applied to deal with the data matrix and leads to a system matrix A. Eigenvalues of A are associated with the dynamic modes of the step response data.

This algorithm was proposed by P. Schmid in 2010 for fluid dynamics analysis [19]. DMD has been applied to real-world phasor measurement unit data collected by ISO New England to identify dynamic modes and reconstruct the measurement [20]. The tool has shown efficacy in identifying modes and reconstructing signals with excellent matching based on the identified modes and their residues.

The main idea of DMD is that the dynamic system under study (in this case, the inverter) is in fact of low order. From the measurement data, a Hankel matrix with a large dimension is formed. This Hankel matrix is closely associated with the system dynamic matrix with a low order; thus, through matrix decomposition using singular value decomposition (SVD) and by keeping only the first n singular values and the associated SVD unitary matrices, a low-rank data matrix is constructed. Further, the system dynamic matrix $\mathbf{A}$ can be recovered by factorizing the low-rank matrix. Readers may refer to [8] and [20] for details of data analytics.

The time-domain expression of a time-domain response $\mathbf{x}(t)$ can also be constructed using the eigenvalues and eigenvectors of $\mathbf{A}$:

$$\mathbf{x}(t) = \sum_{j=1}^{n} \boldsymbol{\phi}_j e^{\omega_j t} b_j = \boldsymbol{\Phi} e^{\boldsymbol{\Omega} t} \mathbf{b}. \tag{7}$$

where $\boldsymbol{\Omega}$ is a diagonal matrix that contains the continuous eigenvalues ω_j., ϕ is the right eigenvector matrix of $\mathbf{A}$, and $\mathbf{b}$ is the initial state projected to the eigenvector basis ($\mathbf{b} = \boldsymbol{\Phi}^{-1} x_0$, where x_0 is the initial state).

The eigenvector matrix, $\boldsymbol{\Phi}$, the eigenvalue matrix, $\boldsymbol{\Omega}$, and the initial state projected to the eigenvector basis, $\mathbf{b}$, will all be identified from the measurement data by DMD.

With the DMD's outputs, $\boldsymbol{\Phi}$, $\mathbf{b}$, and $\boldsymbol{\Omega}$, it is easy to reconstruct the input measurement data using (7) as well as to find the s-domain expression of kth measurement signal as

$$x_k(s) = \sum_{j=1}^{n} \frac{\phi_{kj} b_j}{s - \omega_j}. \tag{8}$$

where $\phi_{kj} b_j$ is the residue of the jth eigenvalue ω_j, n is the order of the system.

Fig. 8 presents both the measurement data (solid lines) and the reconstructed signals (dotted lines). An excellent match has been achieved. With the s-domain expressions for currents found, the admittance model can also be found using (6).

The resulting frequency-domain responses of the admittance models for three operating conditions are compared with the frequency-domain measurements, as shown in Fig. 9.

Remarks:

- Results show that in the frequency range less than 60 Hz, the time-domain data-based admittance models have comparable frequency-domain responses with the frequency-domain measurements.
- Mismatch is obvious for frequency ranges greater than 60 Hz.
- If admittance at a frequency range is small, the time-domain based method leads to more error. This is reasonable because smaller admittance leads to indistinguishable current responses from noise.

V. Insights Obtained from the DQ-domain Admittance Measurements

A. Insight 1: Admittance at Low-Frequency Range Directly Reflecting Operating Conditions

In the dq-frame, the active power, P, and reactive power, Q, exported by the converter and measured at the PCC bus can be expressed as follows:

$$\begin{cases} P = v_d i_d + v_q i_q \\ Q = -v_d i_q + v_q i_d \end{cases} \tag{9}$$

where v and i are the PCC bus voltage and the current measured at the PCC bus.

By linearizing P and Q, the small-signal model is:

$$\begin{bmatrix} \Delta P \\ \Delta Q \end{bmatrix} = \underbrace{\begin{bmatrix} i_d & i_q \\ -i_q & i_d \end{bmatrix}}_{G_1} \begin{bmatrix} \Delta v_d \\ \Delta v_q \end{bmatrix} + \underbrace{\begin{bmatrix} v_d & v_q \\ v_q & -v_d \end{bmatrix}}_{G_2} \begin{bmatrix} \Delta i_d \\ \Delta i_q \end{bmatrix} \tag{10}$$

If we assume that the dq-frame's d-axis is aligned with the PCC voltage's space vector, then $v_d = V$, $v_q = 0$, where V is the magnitude. Also, according to (9), $i_d = \frac{P}{V}$, $i_q = -\frac{Q}{V}$. If the converter is in PQ control mode, in steady state, $\Delta P = 0$ and ΔQ =0.

Eq. (10) becomes the following.

$$\begin{bmatrix} 0 \\ 0 \end{bmatrix} = \underbrace{\frac{1}{V}\begin{bmatrix} P & -Q \\ Q & P \end{bmatrix}}_{G_1} \begin{bmatrix} \Delta v_d \\ \Delta v_q \end{bmatrix} + \underbrace{\begin{bmatrix} V & 0 \\ 0 & -V \end{bmatrix}}_{G_2} \begin{bmatrix} \Delta i_d \\ \Delta i_q \end{bmatrix} \tag{11}$$

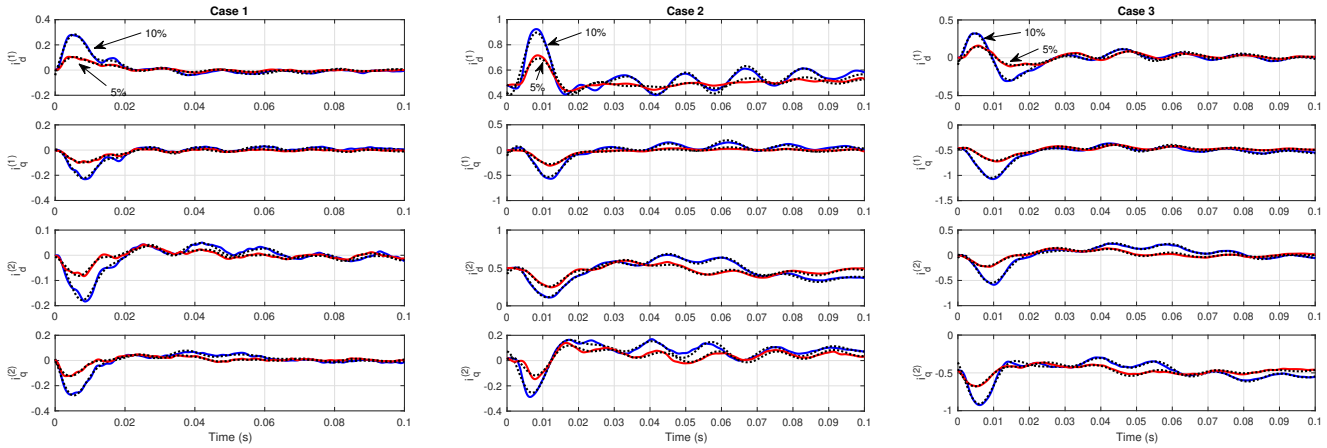

(a) (b) (c)

Fig. 8: Comparison of measurement data (solid lines) and the reconstructed signals (dotted lines). Blue: 10% perturbation. Red: 5% perturbation. (a) Case 1. (b) Case 2. (c) Case 3. Excellent matching is achieved.

Thus, the admittance can be found from (11):

$$0 = \underbrace{\frac{1}{V^2}\begin{bmatrix} P & -Q \\ -Q & -P \end{bmatrix}}_{Y_{\text{VSC}}} \begin{bmatrix} \Delta v_d \\ \Delta v_q \end{bmatrix} + \begin{bmatrix} \Delta i_d \\ \Delta i_q \end{bmatrix} \tag{12}$$

$$\mathbf{Y}_{\text{VSC}} = \frac{1}{V^2}\begin{bmatrix} P & -Q \\ -Q & -P \end{bmatrix}, \ \mathbf{Z}_{\text{VSC}} = \frac{V^2}{|S|^2}\begin{bmatrix} P & -Q \\ -Q & -P \end{bmatrix} \tag{13}$$

Remarks: Equation (13) indicates that in steady state, i.e., 60 Hz in the static frame and 0 Hz in the dq-frame, the DQ-domain admittance directly reflects the operating conditions.

The admittance expression based on steady-state analysis has been investigated in M. Belkhayat's thesis [21]. Although the analysis in [21] is in some ways similar to how we have related the low-frequency response of DQ-domain admittance with the steady-state P and Q values, the admittance expression in [21] is more complicated. The difference between the analysis of [21] and ours lies in two aspects: (i) the assumption of a general dq-frame versus a dq-frame aligned at the PCC bus; (ii) the adoption of real-value versus per unit system.

In this research, we adopt per unit system and a PCC voltage aligned dq-frame. Thus $v_q = 0$ and the expression of admittance is greatly simplified. To the authors' best knowledge, we have not seen anybody explicitly showing this relationship of per-unit values of the admittance matrix at low frequencies related to the per-unit values of P and Q. This insight is valuable as it can directly show the effect of operation point and also serve as a quick sanity-check tool for admittance measurements.

As shown in Fig. 4 and Fig. 6, for Case 4 ($P = 1$ and $Q = 0$), Y_{dd} and Y_{qq} at a very low frequency range (< 1 Hz) have a magnitude of 0 dB or 1 p.u. For Case 2 ($P = 0.5$ and $Q = 0$), Y_{dd} and Y_{qq} at a very low frequency range (< 1 Hz) have a magnitude of -6 dB or 0.5 p.u. In addition, Y_{qq} has a phase angle of 180°, wheras Y_{dd} has a phase angle of 0. Obviously, $Y_{dd} = P$ and $Y_{qq} = -P$ when the PCC voltage is kept at nominal.

For both Case 4 and Case 2, the nondiagonal components have very small magnitudes at the low-frequency range. This fact corroborates $Y_{dq} = Y_{qd} = -Q$ when the PCC voltage is kept at nominal.

For Case 3 ($P = 0$ and $Q = 0.5$), Y_{dq} has a magnitude of -6.8 dB or approximately 0.45 p.u.; and Y_{qd} has a magnitude of -8 dB or 0.40 p.u. According to (13), these two nondiagonal components should have a value of 0.5 p.u. at a low frequency. Note that the admittance refers to the inverter admittance viewed at the PCC point. On the other hand, the measured admittance includes the effect of the transformer. This causes the discrepancy.

For Case 1 ($P = 0$ and $Q = 0$), all four components at a low-frequency range have very small magnitudes. The DQ-domain admittance measurement corroborates the analysis.

B. Insight 2: Detection of Unbalanced Control via Sequence-Domain Admittance

We further proceed to plot sequence-domain admittance to develop more insights. The relationship between the DQ-domain and sequence-domain admittance is as follows [22]:

$$\underbrace{\begin{bmatrix} Y_{pp}(s) & Y_{pn}(s) \\ Y_{np}(s) & Y_{nn}(s) \end{bmatrix}}_{Y_{pn}^m} = \underbrace{\frac{1}{2}\begin{bmatrix} 1 & j \\ 1 & -j \end{bmatrix}}_{H} Y_{dq}^m(s) \underbrace{\begin{bmatrix} 1 & 1 \\ -j & j \end{bmatrix}}_{H^*}. \tag{14}$$

The sequence-domain admittance evaluated at ω_p associates the current phasors at positive sequence of $\omega_p + \omega_1$ and negative sequence $\omega_p - \omega_1$ (where ω_1 is the nominal angular frequency and $\omega_1 = 377$ rad/s) with the respective voltage phasors.

In the low-frequency range, the sequence-domain admittance and impedance are expressed as follows:

$$\mathbf{Y}_{\text{pn}}^{\text{m}} = \frac{1}{V^2}\begin{bmatrix} 0 & P - jQ \\ P + jQ & 0 \end{bmatrix} \tag{15}$$

Fig. 10 presents the sequence-domain admittance measurements. In the low-frequency range, the diagonal components have very small magnitudes, whereas the nondiagonal components have magnitudes and angles corresponding to $P - jQ$ and $P + jQ$, respectively.

Finally, we examine whether unbalanced current control can be reflected in the sequence-domain admittance.

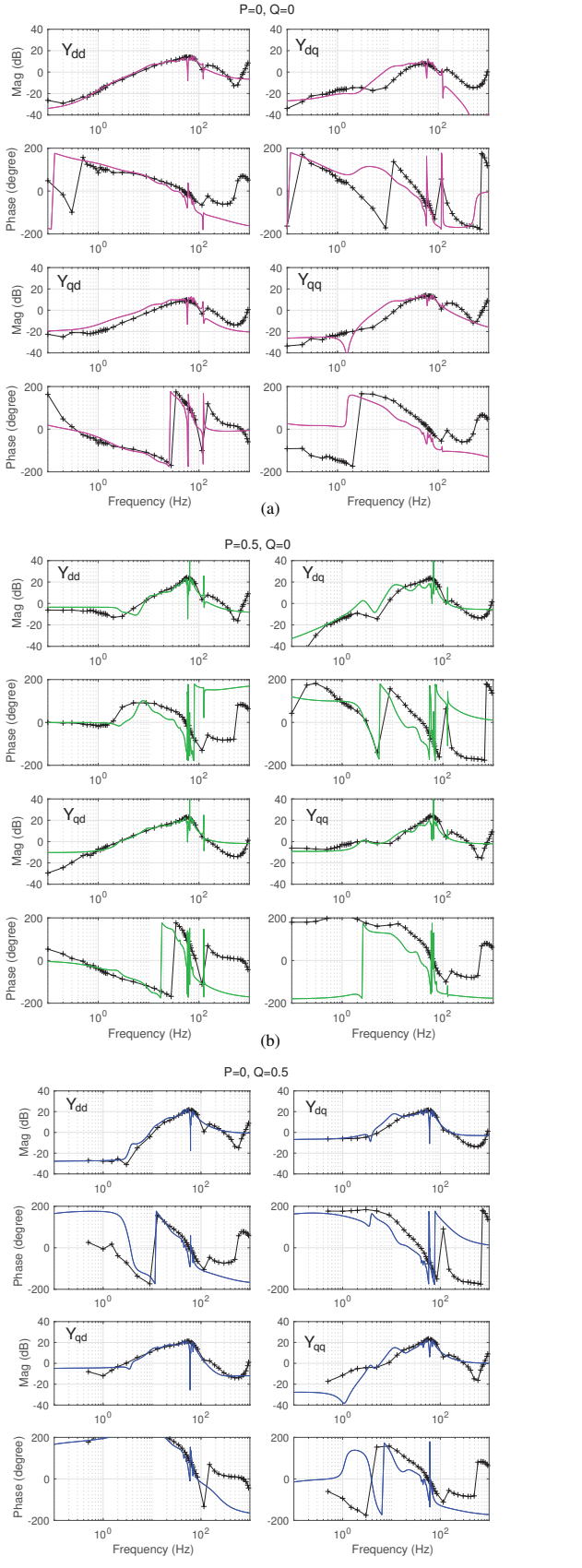

Fig. 9: Comparison of the admittance measurement and the admittance learned from the time-domain data. The system order is assumed to be 16. Solid lines: learned model from step responses. Crosses: discrete frequency-domain measurements.

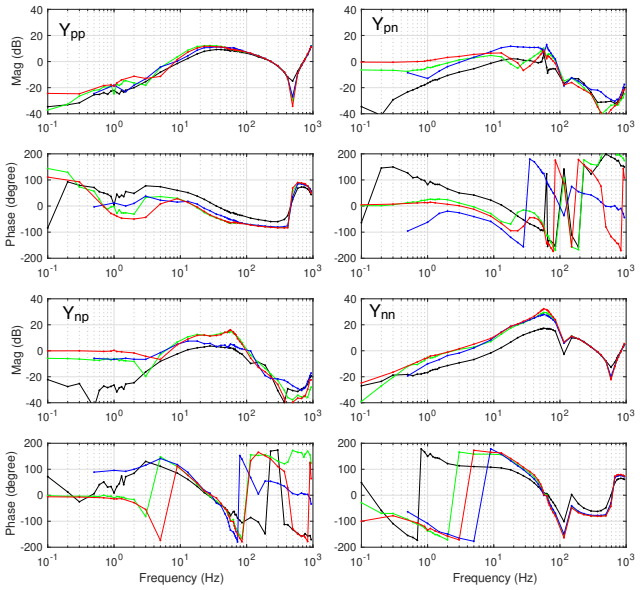

Fig. 10: The sequence-domain admittance viewed at the measurement point.

In particular, we examine sequence-domain admittance at 120 Hz ($\omega_p = 2\pi \times 120$ rad/s). This admittance associates the two current phasors and two voltage phasors. The two voltage (current) phasors are referred to the phasors at positive-sequence 180 Hz and negative-sequence 60 Hz:

$$\begin{bmatrix} \overline{I}_p(j(\omega_p+\omega_1)) \\ \overline{I}_n(j(\omega_p-\omega_1)) \end{bmatrix} = \begin{bmatrix} Y_{pp}(j\omega_p) & Y_{pn}(j\omega_p) \\ Y_{np}(j\omega_p) & Y_{nn}(j\omega_p) \end{bmatrix} \begin{bmatrix} \overline{V}_p(j(\omega_p+\omega_1)) \\ \overline{V}_n(j(\omega_p-\omega_1)) \end{bmatrix} \quad (16)$$

Unbalanced current converter control aims to reduce the negative-sequence current component at 60 Hz when the voltage contains the negative-sequence component. This requirement indicates that the admittance associating the negative-sequence 60-Hz current phasor with the negative-sequence 60-Hz voltage phasor should be small. i.e., $Y_{nn}(s)$ evaluated at 120 Hz should be small.

In Fig. 10, for both Y_{pn} and Y_{nn}, the components of the second column of the admittance matrix, a dip is shown at 120 Hz in the magnitudes. This indicates that the resulting components in the current will be suppressed because of the dip. The dip at 120 Hz observed in Y_{pn} and Y_{nn} also indicates that unbalanced current control is in place.

VI. Conclusion

In this paper, a 2.3-MVA grid-following inverter operating in real and reactive power regulation mode was measured to arrive at its admittance models, under various operating conditions. Two methods —frequency-domain based and time-domain based —are used for cross validation. Both methods can lead to linear models through either vector fitting of frequency-domain data or the DMD-based method to fit the time-domain data. From the frequency-domain admittance measurements, insights of the inverter can be revealed, including its operating condition and whether unbalanced control is included.

REFERENCES

[1] IEEE PES WindSSO Taskforce, "PES TR-80: Wind Energy Systems Subsynchronous Oscillations: Events and Modeling," 2020.

[2] "Technical Report on the events of 9 August 2019," .https://www.ofgem.gov.uk/system/files/docs/2019/09/eso_technical_report_-_final.pdf, 2019.

[3] Joint NERC and WECC Staff. (2019, January) April and May 2018 Fault Induced Solar Photovoltaic Resource Interruption Disturbances Report: Southern California Events: April 20, 2018 and May 11, 2018. NERC.

[4] S. Shah, V. Gevorgian, P. Koralewicz, R. Wallen, and W. Yan, "Impedance methods for analyzing stability impacts of inverter-based resources," in *Proc. 2019 NSF Workshop on Power Electronics Enabled Operation of Power Systems, Chicago, IL, Oct.-Nov*, 2019.

[5] L. Fan and Z. Miao, "Admittance-based stability analysis: Bode plots, nyquist diagrams or eigenvalue analysis?" *IEEE Transactions on Power Systems*, vol. 35, no. 4, pp. 3312–3315, 2020.

[6] J. Huang, K. A. Corzine, and M. Belkhayat, "Small-signal impedance measurement of power-electronics-based ac power systems using line-to-line current injection," *IEEE Transactions on Power Electronics*, vol. 24, no. 2, pp. 445–455, 2009.

[7] B. Badrzadeh, M. Sahni, Y. Zhou, D. Muthumuni, and A. Gole, "General methodology for analysis of sub-synchronous interaction in wind power plants," *IEEE Transactions on Power Systems*, vol. 28, no. 2, pp. 1858–1869, 2012.

[8] L. Fan and Z. Miao, "Time-Domain Measurements-Based DQ-Frame Admittance Model Identification of Inverter-Based Resources," *IEEE Transactions on Power Systems*, pp. 1–1, 2020.

[9] B. Gustavsen and A. Semlyen, "Rational approximation of frequency domain responses by vector fitting," *IEEE Transactions on power delivery*, vol. 14, no. 3, pp. 1052–1061, 1999.

[10] V. Valdivia, A. Lázaro, A. Barrado, P. Zumel, C. Fernández, and M. Sanz, "Impedance identification procedure of three-phase balanced voltage source inverters based on transient response measurements," *IEEE Transactions on Power Electronics*, vol. 26, no. 12, pp. 3810–3816, 2011.

[11] L. Fan and Z. Miao, "A modular small-signal analysis framework for inverter penetrated power grids: Measurement, assembling, aggregation, and stability assessment," *arXiv preprint arXiv:2003.03860*, 2020.

[12] Z. Staroszczyk, "A method for real-time, wide-band identification of the source impedance in power systems," *IEEE Transactions on Instrumentation and Measurement*, vol. 54, no. 1, pp. 377–385, 2005.

[13] M. Céspedes and J. Sun, "Online grid impedance identification for adaptive control of grid-connected inverters," in *2012 IEEE Energy Conversion Congress and Exposition (ECCE)*. IEEE, 2012, pp. 914–921.

[14] Z. Shen, M. Jaksic, P. Mattavelli, D. Boroyevich, J. Verhulst, and M. Belkhayat, "Three-phase ac system impedance measurement unit (imu) using chirp signal injection," in *2013 Twenty-Eighth Annual IEEE Applied Power Electronics Conference and Exposition (APEC)*. IEEE, 2013, pp. 2666–2673.

[15] T. Roinila, M. Vilkko, and J. Sun, "Broadband methods for online grid impedance measurement," in *2013 IEEE Energy Conversion Congress and Exposition*. IEEE, 2013, pp. 3003–3010.

[16] T. Roinila and T. Messo, "Online grid-impedance measurement using ternary-sequence injection," *IEEE Transactions on Industry Applications*, vol. 54, no. 5, pp. 5097–5103, 2018.

[17] S. Shah, P. Koralewicz, V. Gevorgian, and R. Wallen, "Impedance measurement of wind turbines using a multimegawatt grid simulator,," in *Proc. Of 18th Wind Integration Workshop, Dublin, Ireland*, 2019.

[18] B. Ho and R. E. Kálmán, "Effective construction of linear state-variable models from input/output functions," *at-Automatisierungstechnik*, vol. 14, no. 1-12, pp. 545–548, 1966.

[19] P. J. Schmid, "Dynamic mode decomposition of numerical and experimental data," *Journal of fluid mechanics*, vol. 656, pp. 5–28, 2010.

[20] A. Alassaf and L. Fan, "Randomized dynamic mode decomposition for oscillation modal analysis," *IEEE Transactions on Power Systems*, 2020.

[21] M. Belkhayat, "Stability criteria for ac power systems with regulated loads," Ph.D. dissertation, Purdue University West Lafayette, NI, 1997.

[22] S. Shah and L. Parsa, "Impedance modeling of three-phase voltage source converters in dq, sequence, and phasor domains," *IEEE Transactions on Energy Conversion*, vol. 32, no. 3, pp. 1139–1150, 2017.

Lingling Fan (SM'08) received the B.S. and M.S. degrees in electrical engineering from Southeast University, Nanjing, China, in 1994 and 1997, respectively, and the Ph.D. degree in electrical engineering from West Virginia University, Morgantown, in 2001. Currently, she is a full professor at the University of South Florida, Tampa, where she has been since 2009. She was a Senior Engineer in the Transmission Asset Management Department, Midwest ISO, St. Paul, MN, form 2001 to 2007, and an Assistant Professor with North Dakota State University, Fargo, from 2007 to 2009. Her research interests include power systems and power electronics. Dr. Fan serves as the editor-in-chief for IEEE Electrification Magazine and associate editor for IEEE Trans. Energy Conversion.

Zhixin Miao (SM'09) received the B.S.E.E. degree from the Huazhong University of Science and Technology,Wuhan, China, in 1992, the M.S.E.E. degree from the Graduate School, Nanjing Automation Research Institute (Nanjing, China) in 1997, and the Ph.D. degree in electrical engineering from West Virginia University, Morgantown, in 2002.

Currently, he is with the University of South Florida (USF), Tampa. Prior to joining USF in 2009, he was with the Transmission Asset Management Department with Midwest ISO, St. Paul, MN, from 2002 to 2009. His research interests include power system stability, microgrid, and renewable energy.

Przemyslaw Koralewicz (M'17) received the M.S.E.E. degree from Silesian Technical University, Gliwice, Poland, in 2010. He specializes in modeling, detailed analysis, and testing of smart inverters and complex power systems including microgrids. He is utilizing the National Renewable Energy Laboratory Controllable Grid Interface, a new, groundbreaking testing apparatus and methodology to test and demonstrate many existing and future advanced controls for various renewable generation technologies on the multimegawatt scale and medium-voltage levels.

Shahil Shah (S'13-M'18) received the B.E. degree from Government Engineering College, Gandhinagar, India, in 2006, the M.Tech. degree from the Indian Institute of Technology Kanpur, Kanpur, India, in 2008, and the Ph.D. degree from Rensselaer Polytechnic Institute (RPI), Troy, NY, USA, in 2018, all in electrical engineering.,Before joining the Ph.D. program with RPI in 2012, he worked with Bhabha Atomic Research Center, Siemens Corporate Technology, and GE Global Research Center, India. He is currently a Research Engineer with the Power Systems Engineering Center, the National Renewable Energy Laboratory, Golden, CO, USA. His research interests include applications of modeling and control for dynamic and transient stability of power systems with high penetration of renewable generation.,Dr. Shah was the recipient of the 2018 RPI Allen B. Dumont prize, given to a Doctoral Candidate "who demonstrates high scholastic ability and makes substantial contribution to his/her field."

Vahan Gevorgian (M'97–SM'17) received the Ph.D. degree in electrical engineering from the State Engineering University of Armenia, Yerevan, Armenia, in 1993. He joined National Renewable Energy Laboratory (NREL) in October 1994 and has served many roles over the years. He is currently working with the Power Systems Engineering Center focused on renewable energy impacts on transmission and interconnection issues and dynamic modeling of variable generation systems. He research interests include dynamometer and field testing of large and small wind turbines, dynamometer testing of wind turbine drivetrain components, development of advanced data acquisition systems, and wind turbine power quality. He provides technical support to NREL industry partners and major U.S. wind turbine manufacturers. He is member of the IEC Team for wind turbine power quality standards. His contributions to NREL research have been recognized through multiple Outstanding Individual and Team Staff awards.